Experimental Eye Research 234 (2023) 109616

Contents lists available at ScienceDirect

Experimental Eye Research

journal homepage: www.elsevier.com/locate/yexer

Research article

Retinal ganglion cells encode differently in the myopic mouse retina?

Qin Wang [a,b,2], Chunghim So [a,2], Bing Zuo [a], Seema Banerjee [a,1], ChunTing Qiu [a], Zhang Ting [a,b,d], Allen Ming-Yan Cheong [a,b], Dennis Yan-yin Tse [a,b], Feng Pan [a,b,c,d,*]

[a] School of Optometry, The Hong Kong Polytechnic University, Kowloon, Hong Kong
[b] Centre for Eye and Vision Research (CEVR), 17W Hong Kong Science Park, Hong Kong
[c] Research Centre for SHARP Vision (RCSV), The Hong Kong Polytechnic University, Hong Kong
[d] Hong Kong Polytechnic University Shenzhen Research Institute, Hong Kong

ARTICLE INFO

Keywords:
Retinal ganglion cells (RGCs)
Myopia
Retina
Vision
Machine learning

ABSTRACT

The etiology of myopia remains unclear. This study investigated whether retinal ganglion cells (RGCs) in the myopic retina encode visual information differently from the normal retina and to determine the role of Connexin (Cx) 36 in this process. Generalized linear models (GLMs), which can capture stimulus-dependent changes in real neurons with spike timing precision and reliability, were used to predict RGCs responses to focused and defocused images in the retinas of wild-type (normal) and Lens-Induced Myopia (LIM) mice. As the predominant subunit of gap junctions in the mouse retina and a plausible modulator in myopia development, Cx36 knockout (KO) mice were used as a control for an intact retinal circuit. The kinetics of excitatory postsynaptic currents (EPSCs) of a single αRGC could reflect projection of both focused and defocused images in the retinas of normal and LIM, but not in the Cx36 knockout mice. Poisson GLMs revealed that RGC encoding of visual stimuli in the LIM retina was similar to that of the normal retina. In the LIM retinas, the linear-Gaussian GLM model with offset was a better fit for predicting the spike count under a focused image than the defocused image. Akaike information criterion (AIC) indicated that nonparametric GLM (np-GLM) model predicted focused/defocused images better in both LIM and normal retinas. However, the spike counts in 33% of αRGCs in LIM retinas were better fitted by exponential GLM (exp-GLM) under defocus, compared to only 13% αRGCs in normal retinas. The differences in encoding performance between LIM and normal retinas indicated the possible amendment and plasticity of the retinal circuit in myopic retinas. The absence of a similar response between Cx36 KO mice and normal/LIM mice might suggest that Cx36, which is associated with myopia development, plays a role in encoding focused and defocused images.

1. Introduction

Myopia (near-sightedness), a significant public health problem, affects at least 80% of adults in Hong Kong and 28% of the global population (Baird et al., 2020; Foster and Jiang, 2014; Holden et al., 2016; Vitale et al., 2008). The latter percentage is estimated to increase to 50% by 2050 (Holden et al., 2016). Despite its prevalence, the specific entity (ies) responsible for normal refraction or myopia remains elusive.

Emmetropia is a developmental process by which the eye's optical power matches its axial length. The process is regulated by defocused images associated with eye growth and refraction (Smith and Hung, 1999; Smith et al., 2013). In myopic eyes, an elongated axial length results in distant images focusing in front of the photoreceptors. These projected defocused images have different light intensities, projected areas and blurred edges compared to focused images (Pan, 2019), which are known to induce eye growth and contribute to myopia. The retina, which conveys visual information to the brain by retinal ganglion cells (RGCs), can sense the focus plane of an image and may play a role in myopia development (Schaeffel and Wildsoet, 2013). Understanding whether the myopic retina encodes visual information differently from the emmetropic retina could provide potential targets for myopia control in the retina.

RGCs can reliably and swiftly code visual information when the retinal circuit is intact (Gollisch, 2009). After receiving signals from multiple cell types, including bipolar and amacrine cells within the

* Corresponding author. School of Optometry, The Hong Kong Polytechnic University, Hung Hom, Hong Kong.
E-mail address: feng.a.pan@polyu.edu.hk (F. Pan).
[1] Current address: Department of Ophthalmology and Genetics, Wilmer Eye Institute, The Johns Hopkins University, School of Medicine, USA.
[2] These authors contributed equally to this work.

https://doi.org/10.1016/j.exer.2023.109616
Received 7 March 2023; Received in revised form 6 August 2023; Accepted 11 August 2023
Available online 12 August 2023

Abbreviations

AIC	Akaike information criterion
AL	Axial length
Cx36	Connexin 36
d	Day
D	Diopter
EPSCs	Excitatory postsynaptic currents
GLMs	Generalized linear models
KO	Knock out
LIM	Lens-Induced myopia
LNP	linear-nonlinear-Poisson
RGCs	Retinal ganglion cells
RE	Refractive Error
RPE	Retinal pigment epithelium
SD-OCT	Spectral-domain–optical coherence tomography
S.E.M.	Standard error of the mean
WT	Wild-type

mammalian retina (Masland, 2012), RGCs compute and extract features of visual information (Gollisch and Meister, 2010). The signaling cascades and the visual signaling delivered from the RGCs to the optic nerve in the myopic retina could be changed (Banerjee et al., 2020). Research had shown that a defocused image projected in front of the retina mimicking the myopic status could alter the firing patterns of RGCs (Banerjee et al., 2020; Pan, 2019). After the intervention, a modified retinal signalling cascade was observed in the LIM retina, ranging from hours to days (Wu et al., 2018). It remains unclear, however, whether the change of the firing patterns of RGCs in the myopic retina affected the coding of visual information, potentially causing the information to be represented differently than in a normal retina. If the coding of RGCs in the myopic retina is distinct from that in the normal retina, this would suggest that the circuitry of the myopic retina has undergone modifications. To test the difference, a computational model will be applied.

Computational models based on the current understanding of the intact retinal circuit can provide quantitative predictions of responses to a range of visual stimuli. The most common approach to describing spatio-temporal correlations and visual signalling in neuronal populations is the receptive field associated with white noise stimuli (Hubel and Wiesel, 1968; Pillow et al., 2008). However, this model may be inadequate for estimating neural spike responses (Troy and Lee, 1994). Generalized linear models (GLMs), which are comprised of a set of linear filters and point nonlinearity, are simple yet flexible models that can capture actual neuronal response properties. GLMs can be applied to fit and analyze spike trains from electrophysiological recordings with desirable statistical properties (Weber and Pillow, 2017).

This study aimed to determine whether the biophysical activities of single RGC in both normal and LIM retinas differed in encoding focused/defocused images by fitting with a GLM model. The predicted responses of RGCs from both WT and LIM retinas to focused and defocused images, which mimic the normal and myopic states, were compared and analyzed at the cellular level. Any discrepancies between the model prediction and the actual responses could indicate the entity(ies) responsible for normal refraction or myopia.

Measuring focused/defocused images from RGC spike trains may require more computation than from the photoreceptor level, similar to the temporal encoding of sensory neurons in computing complex visual features and nonlinear circuit dynamics in the retina to contribute to computing motion trajectory (Gutig et al., 2013; Leonardo and Meister, 2013). The encoding process may necessitate that the downstream visual area first decodes the RGC signals using an internal retina model (Pillow et al., 2005, 2008). After reading the input image from the photoreceptor output, further computation could be necessary in the internal myopic retina. Alternatively, the RGCs may have already computed the focused image, which could explain why the RGC's responses appear so intricate, consisting of multiple bursts of action potentials (Crapper and Noell, 1963; Granit, 1946). If this were the case, the downstream circuits could calculate the focused image through a simple transformation of the RGC output largely independent of the internal dynamics of the retina. The brain could use either or both solutions. While much work has successfully characterized the sophisticated decoding approach to retinal signals (Botella-Soler et al., 2018), the calculations that refine the RGC output in the myopic retina have received less attention, particularly in terms of how images are processed by circuits in the myopic retina. If the retina was capable of performing computations that permit simple downstream processing, it would be interesting to identify what differences exist between the normal and myopic retina.

The study focused on investigating the biophysiological properties of Alpha retinal ganglion cells (αRGCs), which play a crucial role in visual processing. This was evident from their large somas, broad dendritic fields, and mosaic-like spacing in the retina, despite functional differences observed in each subtype.(Krieger et al., 2017; Peichl, 1991).

Gap junctions are a key component of the intact retinal circuit, enabling signal averaging and synchronization in the retina. (Bloomfield and Volgyi, 2004). The predominant subunit of gap junctions in the proximal mouse retina is Connexin (Cx) 36, which is expressed by most RGC subtypes (Pan et al., 2010). Recent studies on myopia have demonstrated that single nucleotide polymorphisms (SNPs) in the GJD2 gene, which encodes for the Cx36 protein, are highly expressed and considered plausible modulators in myopia development (Quint et al., 2021; Verhoeven et al., 2013). Our previous research revealed increased phosphorylation of Cx36 of AII amacrine cells in the myopic retina (Banerjee et al., 2020). These findings suggest that Cx36 is somehow associated with refractive error and that a myopic retina with an altered or adapted signaling cascade could lead to modifications in the encoding of RGCs, resulting in an effective adjustment to the retinal circuitry. Cx36 knockout mice were used as a control to investigate the effects of its deficiency in the retinal circuit (Pan et al., 2010).

Overall, the study highlighted the vital importance of a functioning neural circuit in the retina and suggested that the encoding of visual information in a myopic retina might differ from that of a normal retina.

2. Methods

2.1. Animal preparation

All procedures involving mice in this study were approved by the Animal Subjects Ethics Sub-Committee of the Hong Kong Polytechnic University (Approval number: 20–21/128-SO-R-GRF). The study complied with the Guide for the Care and Use of Laboratory Animals published by the National Institutes of Health.

Adult wild-type (WT) mice of either sex (postnatal day 16–56) C57BL/6J (RRID: IMSR_JAX:000664), weighing (15–20 grams), were used (n = 56). Kcng4-YFP (6–8 weeks, n = 11) mice (Duan et al., 2015) of either sex, weighing (15–25 grams), were used for ON and OFF αRGC labeling as previously described (Wang et al., 2020). Homozygous *Cx36*-knockout (KO) mice (RRID: MGI:3810172), first generated in the laboratory of David Paul, Harvard Medical School (Cambridge, MA), were a kind gift from Samuel M. Wu, Baylor College of Medicine (n = 6, aged 6–8 weeks, weight 15–25 grams). All animals were maintained in a 12-h light/12-h dark cycle. The mice were deeply anesthetized with an intraperitoneal injection of ketamine and xylazine [80 mg/kg and 10 mg/kg (body weight), respectively], and lidocaine hydrochloride (20 mg/ml) was applied locally to the eyelids and surrounding tissues before enucleation. Retinas were collected around 10 a.m. for consistency.

2.2. Lens-induced myopic (LIM) mouse model

Myopia was induced using the previously described lens-induced method (LIM)(Jiang et al., 2018). In brief, custom-made −30 diopter (D) lenses made of poly(methyl methacrylate) (PMMA) were fitted into spectacle frames (Fig. 1A). The left untreated eye was a control, while the right eye induced myopia. The spectacles were fitted onto mice at postnatal day 21, worn for five weeks, and removed twice weekly for cleaning.

At the end of this period, refraction and axial length (AL) were measured for each eye on the same day. Retinas were then harvested for further processing and analysis.

2.3. Refraction measurements in mouse model

Refractive error (RE) was measured using an infrared photorefractor (Steinbeis Transfer Center, Stuttgart, Germany) (Schaeffel, 2008). To decrease movement and to obtain accurate RE measurements, mice were lightly anesthetized with an intraperitoneal injection of ketamine (Vedno, St. Joseph, MO, United States) and xylazine (Akorn, Decatur, IL, United States) [10 and 1 mg (kg body weight) $^{-1}$, respectively]. The eyes were instilled with tropicamide, phenylephrine hydrochloride solution (Mydrin-P ophthalmic solution; Santen Pharmaceutical Co., Ltd., Osaka, Japan) 10 min before the measurement to ensure mydriasis and cycloplegia. Twenty measurements were taken along the optical axis for each eye, and the averages were calculated (Fig. 1B). However, refraction measurements obtained by the infrared photorefractor showed considerable variation. To confirm the myopic status of the LIM, the axial length (AL) was measured using spectral-domain–optical coherence tomography (SD-OCT, Bioptigen Spectral Domain Ophthalmic Imaging System, Envisu R4410 SD-OCT Leica Microsystems, Wetzlar, Germany) under light anesthesia. The anesthetized mouse was placed in a cylindrical holder attached to an X-Y-Z movable stage in front of the SD-OCT light source. Streak retinoscopy was also performed to confirm refractive error measurements. Any animal with >5D difference between photorefractor and retinoscopy measures was excluded.

Corneal curvature was measured using the infrared photorefractor to rule out corneal damage in the model (Schaeffel, 2008).

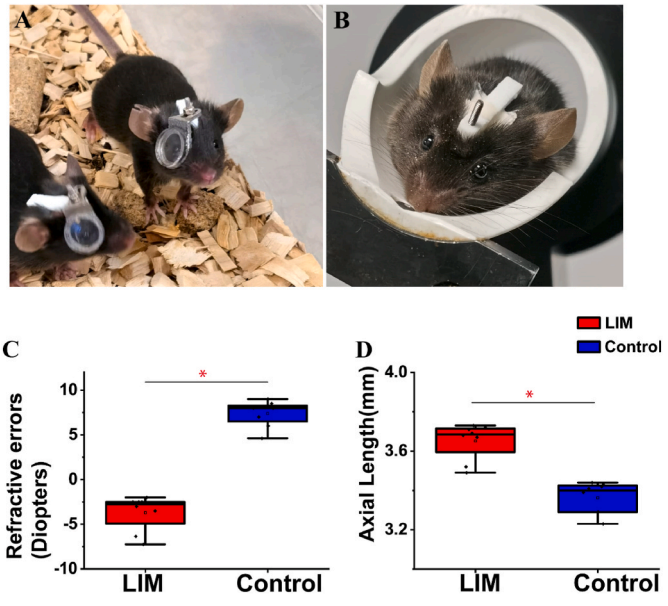

Fig. 1. Lens-Induced Myopia (LIM) mouse and Optical Coherence Tomography (OCT) measurement. A: The image shows a LIM mouse wearing skull-mounted eyeglasses. B: Refraction measurements were taken of the LIM mouse eye while the mouse was under light anaesthesia to ensure stable results. Refraction errors were measured in awake mice. C: Photorefraction was used to measure mice's refractive errors (RE). The red star shows a significant difference between the eyes of LIM mice and control (untreated) eyes. D: Optical Coherence Tomography (OCT) was used to measure the axial length of the mouse eye, from the corneal surface to the retinal pigment epithelium layer. (For interpretation of the references to color in this figure legend, the reader is referred to the Web version of this article.)

2.4. Flattened retina preparation

Anesthetized animals were euthanized by cervical dislocation immediately after enucleation. The eyes were removed from animals under dim red illumination. The retinas from the dorsal section of the mid-peripheral retina in the nasotemporal plane were used for patch-clamp recordings and attached to a modified translucent Millicell filter ring (Millipore, Bedford, MA). The flattened retinas were superfused with oxygenated mammalian Ringer's solution (Bloomfield and Miller, 1982). The bath solution was continuously bubbled with 95% O_2–5% CO_2, while being maintained at approximately 32 °C, as previously described (Pan et al., 2016; Volgyi et al., 2013).

2.5. Patterned light stimulation

A green organic light-emitting display (OLED) (OLEDXL, Olightek, Kunming, Yunnan, China; 800 × 600-pixel resolution, 85 Hz refresh rate) was controlled by an Intel Core Duo computer with a Windows 7 operating system. Using a Nikon 40x water-immersion objective (CFI Apo 40XW NIR, NA = 0.8), the area of the retina that received light stimuli was 250 μm in diameter. Under the 40x objective, the 15 μm diameter pixels of the OLED presented 0.25 μm/pixel on the retina. Spatial frequency stimuli generated by PsychoPy (University of Nottingham, UK) were projected onto the photoreceptor layer. The background light intensity was ~700 photoisomerizations per rod per second (Rh*/rod/s), and the highest stimulus was ~1.816×10^5 Rh*/rod/s. At this background illumination level, the rod pathway is saturated, leaving the cone pathway to mediate the light response (Borghuis et al., 2013). All images were produced by a 1-s stimulation followed by a 5-s interval. A focused/defocused 125 μm diameter of 0.0067 cycles/degree image was applied from Figs. 2, 4 and 5 and Supplementary Figs. 2 and 3.

The details of the system used to generate defocused images have been previously published (Pan, 2019). The custom-made light--projected system was made to project images onto the photoreceptor cells layer using a physical movable lens, rather than digital blurring. It has been calculated that an axial elongation of 5 μm would induce 1 Diopter (D) refractive error in the mouse retina (Schaeffel, 2008). Therefore, 100 μm defocus would be expected to induce plus or minus 20 diopters refractive error under microscopy, depending on the direction of defocus.

The nature scenes pictures (Fig. 7) are cited from Google and converted to grayscale using Adobe Photoshop 7 (Aadobe Inc, San Jose, CA, USA). These nature pictures were used to test the RGC responses to images containing various subjects, including landscapes, people, and animals.

2.6. Electrophysiology

Extracellular and whole-cell recordings were performed using an Axopatch 700B amplifier connected to a Digidata 1550B interface and pCLAMP 10 software (Molecular Devices, San Jose, CA). Cells were visualized with near-infrared light (>775 nm) at 40 × magnification with a Nuvicon tube camera (Dage-MTI, Michigan City, IN) and differential interference optics on a fixed-stage microscope (Eclipse FN1; Nikon, Tokyo, Japan). The retinas were superfused at a rate of 1–1.5 ml min^{-1} with Ringer's solution containing: 120 mM NaCl, 2.5 mM KCl, 25 mM $NaHCO_3$, 0.8 mM Na_2HPO_4, 0.1 mM NaH_2PO_4, 1 mM $MgCl_2$, 2 mM $CaCl_2$, and 5 mM D-glucose. The bath solution was continuously bubbled with 95% O_2–5% CO_2 at 32 °C. Electrodes were pulled to 5−7 MΩ

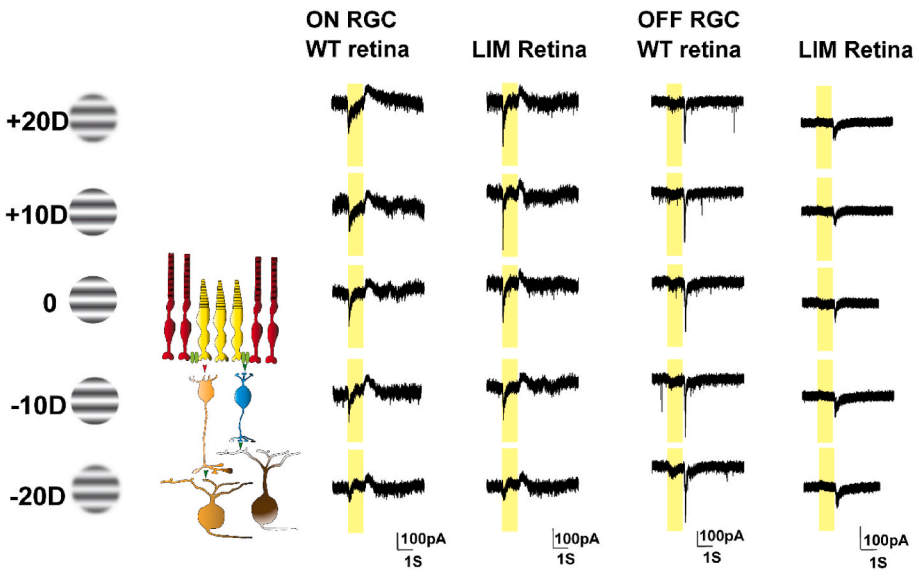

Fig. 2. Schematic of the responses of ON and OFF αRGCs to focused and defocused image stimuli. A focused 125 μm diameter of 0.0067 cycles/degree image was projected onto the outer segment of photoreceptors. The focused image is defined as 0 diopters. Subsequently, defocused images under the microscope equal to ±10 and ± 20 diopters images were projected onto different retinal layers, according to the calculation that 5 μm of defocus could induce a refractive error of plus or minus 1 diopter (Schaeffel, 2008). The light intensities ranged from 3.74 x10^4 Rh*/rod/sec to 3.85 x10^4 Rh*/rod/sec. Whole-cell light responses of ON and OFF αRGCs were recorded and analyzed from LIM and normal (Wild-Type, WT) retinas.

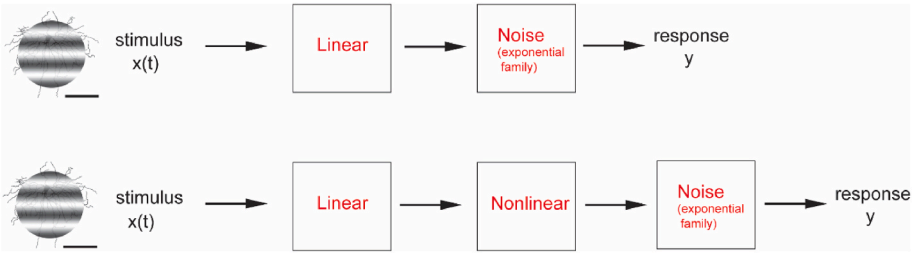

Fig. 3. Schematic of generalized linear encoding model (GLM). The upper figure shows a linear model.
The lower figure shows a linear-nonlinear-Poisson (LNP) model. The model comprises a linear filter to describe how the neuron integrates the stimulus over time and space; a point nonlinearity to transform filter output into the neuron's response range; and exponential-family noise to capture stochasticity in the responses.

resistance, with internal solution consisting of 120 mM potassium gluconate, 12 mM KCl, 1 mM $MgCl_2$, 5 mM EGTA, 0.5 mM $CaCl_2$, and 10 mM HEPES (adjusted to pH 7.4 with KOH). This internal solution was used in experiments to avoid blockage of spiking. To improve the space clamp and to block spiking, the whole-cell excitatory postsynaptic potentials (EPSPs) were recorded with an internal solution containing cesium methanesulfonate instead of potassium gluconate. The chloride equilibrium potential (ECl) with these internal solutions was approximately −63 mV.

Spike trains were recorded digitally at a sampling rate of 10 kHz using Axoscope software (Molecular Devices), and sorted using an Offline Sorter (Plexon, Dallas, TX) and NeuroExplorer (Nex Technologies, Littleton, MA, USA) software. In the whole-cell recording, the kinetics of excitatory postsynaptic currents (EPSCs), including the area bounded by the trace and the baseline, time, and slope of Maximal rise (decay)(the slope from within the region bounded by the start of the search region and the peak) of EPSPs, were measured and compared. For comparison purposes, the spike frequencies were normalized. The recorded cells were dye-injected using pipette tips filled with 4% Neurobiotin (Vector Laboratories, Burlingame, CA, USA) and 0.5% Lucifer Yellow-CH (Molecular Probes, Eugene, OR, USA), as previously described (Pan and Massey, 2007).

2.7. Immunohistochemistry staining

After recording, the retinal pieces attached with filter paper (RGCs up) were submersion-fixed in 2% N-(3-dimethylaminopropyl)-N′-ethyl-carbodiimide hydrochloride ("carbodiimide"; Sigma-Aldrich, Burlington, MA, USA) in 0.1 M phosphate buffer (PB) saline, pH 7.5, for 30 min at room temperature. Following fixation, the retinas were separated from the filter paper, extensively washed with 0.1 M PB (pH 7.4), and blocked with 3% donkey serum in 0.1 M PB with 0.5% Triton-X 100 and 0.1% NaN3 overnight. The primary antibodies were then diluted in 0.1 M PB with 0.5%Triton-X 100 and 0.1% NaN3, containing 1% donkey serum. The tissues were incubated with primary antibodies for 3–7 days at 4 °C and, after extensive washing, incubated with secondary antibodies overnight at 4 °C. The tissues were then washed with 0.1 M PB and mounted in Vectashield (Vector Laboratories) for observation.

The ON and OFF αRGCs were confirmed by Neurobiotin injection, as previously reported (see Supplementary Fig. 1)(Wang et al., 2021). Before immunohistochemical staining, the retinal pieces were fixed in 4% paraformaldehyde for at least 10 min. The retina tissues were then incubated with choline acetyltransferase (ChAT, goat anti-ChAT, 1:500; Millipore- Sigma, Billerica, MA, USA; Cat# AB144P, RRID: AB_2079751) antibody for 3–7 days at 4 °C, followed by incubation with the secondary antibodies overnight at 4 °C. After washing with 0.1 M phosphate-buffered saline (PBS), the tissues were mounted for observation and image capture under a Zeiss LSM 800 with an Airyscan confocal microscope (ZEISS, Thornwood, NY) using a 43 × objective (NA 1.3).

2.8. Data acquisition and analysis

Statistical analyses were performed using Origin software (OriginLab, Northampton, MA). Statistically, significant differences ($P < 0.05$) were determined by the Student t-test. Unless otherwise indicated, the results are shown as mean values ± standard error of the mean (SEM).

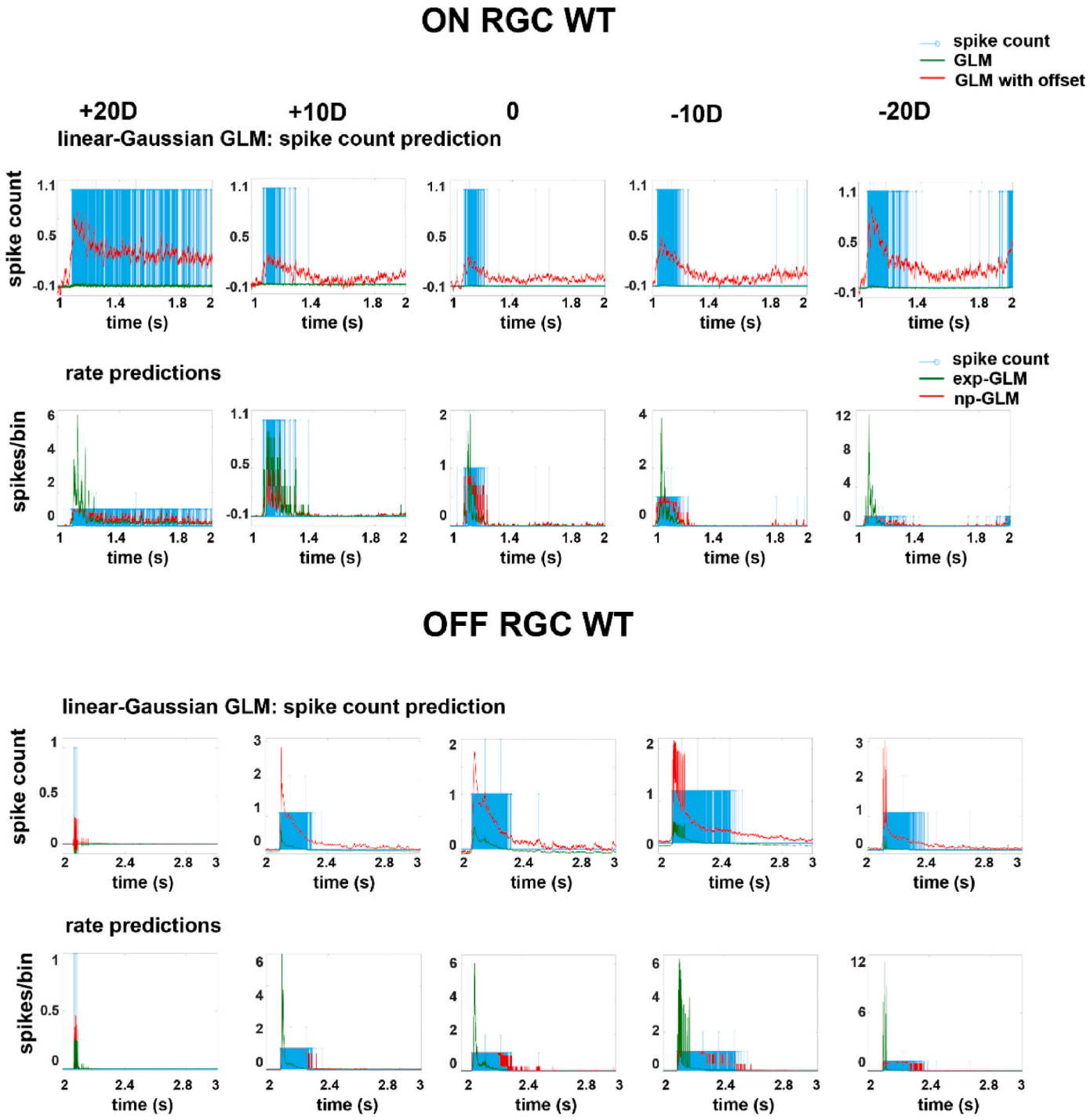

Fig. 4. GLM models applied in ON and OFF αRGCs analyses in normal (WT) retinas. GLM models can be applied to predict the spike count (upper row) and rate (lower row) under focused and defocused image projections of different power. X axis: time in seconds; y axis: spike count in spike count prediction and spikes per bin in rate predications.

2.9. Generalized linear model

Generalized linear models (GLM) have previously been applied to spike representations in the visual system, known as the Linear-nonlinear-Poisson (LNP) model (Pillow et al., 2008; Truccolo et al., 2005). Poisson generalized linear models (GLMs) are defined by a weight vector k that filters the stimulus, a set of linear filters, a nonlinear function, and noise from an exponential family distribution (Fig. 3), with statistical properties for fitting. Each cell's input is described by a set of filters: a stimulus filter and a post-spike filter, which captures dependencies on spike-train history. The summed filter responses are exponentiated for each neuron to obtain an instantaneous spike rate. GLMs can capture stimulus-dependent changes in spikes with time precision and reliability that mimic those in real neurons (Weber and Pillow, 2017).

In this study, ON or OFF αRGCs in the *in vitro* mouse retina were recorded while different powers of defocused/focused images were presented on the receptive field of the neuron. GLM models were then applied to predict the spike count, rate, spike times, and spike trains under focused and different power-defocused image projections. The

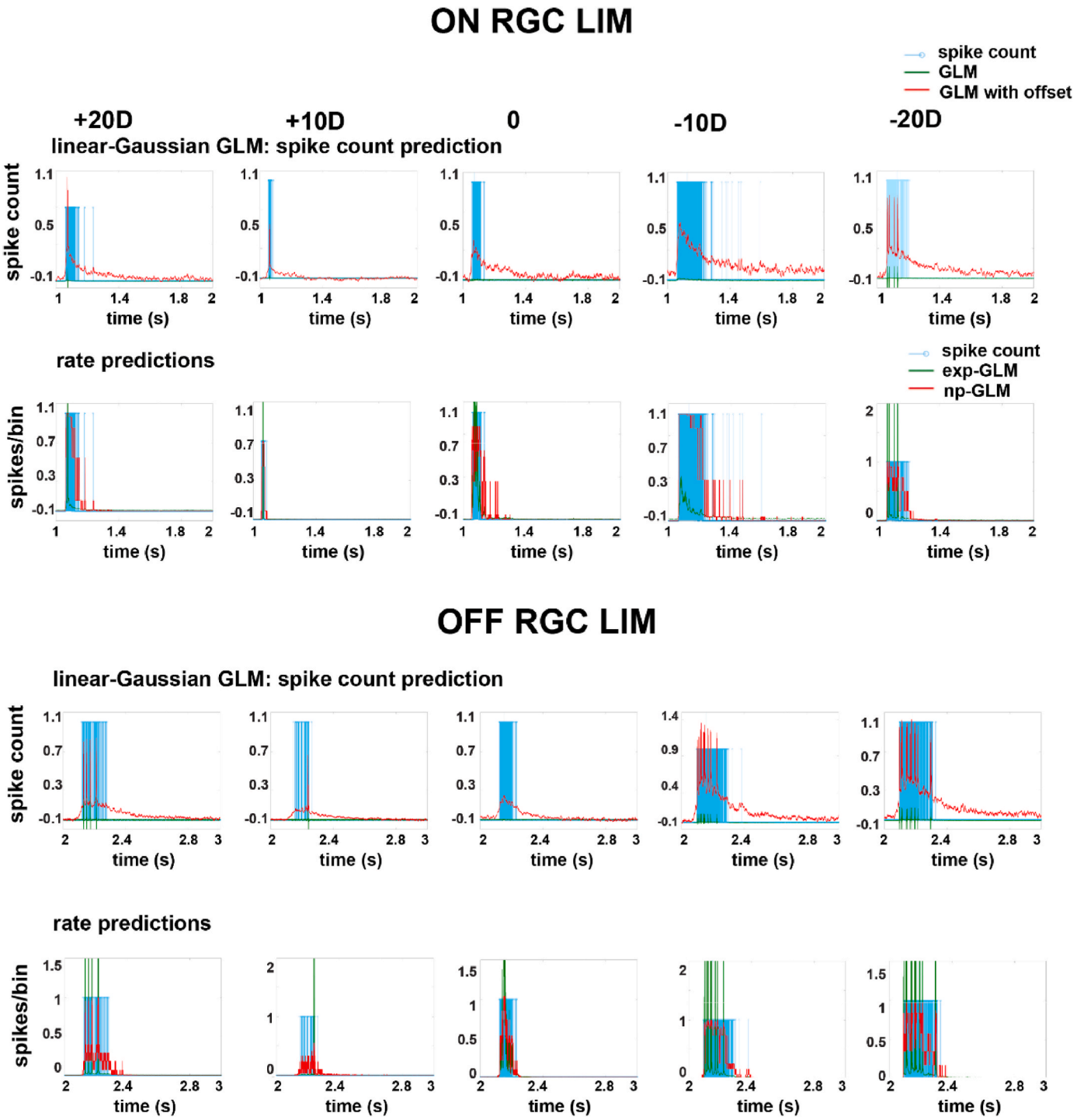

Fig. 5. GLM models applied in ON and OFF αRGCs analyses in LIM retinas. GLM models are applied to predict the spike count (upper row) and rate (lower row) under focus and defocused image projections of different power. X axis: time in seconds; y axis: spike count in spike count prediction and spikes per bin in rate predications.

linear step of the cascade processes the stimulus with a linear k, whose output reflects the degree to which the stimulus s(t) matches k. The baseline offset (y-intercept) was set in linear regression. The nonlinear step acts on the output of the receptive field, ks(t), which is scaled by a nonlinear function that could include the effects of spike threshold and response saturation. The linear and the nonlinear filters fit the data to improve the firing rate prediction. This model consisted of a linear filter k, which describes how the neuron integrates the stimulus over time and space, followed by a point nonlinearity, which transforms the filter output into the neuron's response range, and exponential-family noise that captures stochasticity in the response (El Hady, 2016; Paninski, 2004).

The Poisson GLM is given by

$$\lambda = g(k^{\top}x),\ r|x \sim \mathrm{Poiss}(\Delta\lambda),$$

where $k^{\top}x$ is the dot product between the filter k and the stimulus x, the nonlinearity g ensures the spike rate λ is nonnegative, and Δ is a time bin size. The model can be extended to incorporate linear dependencies on

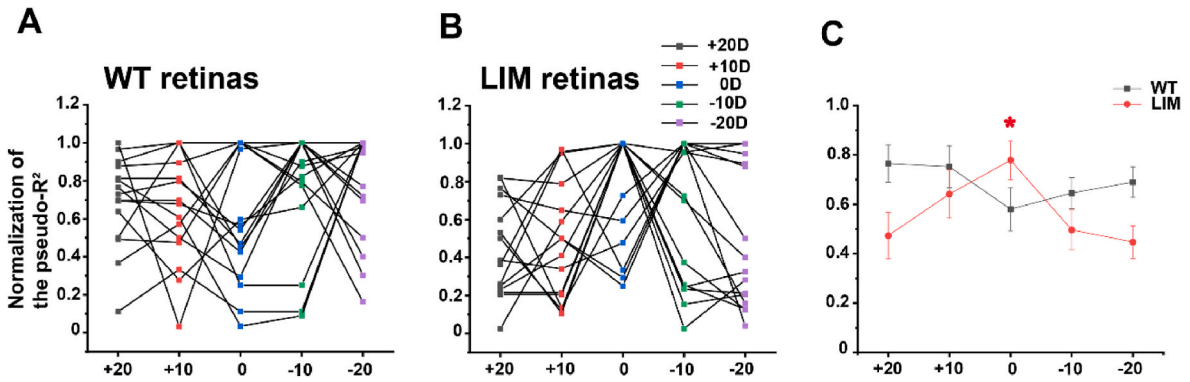

Fig. 6. Pseudo-R^2 in linear-Gaussian-GLM model with offset to predict the spike count. **A**: In normal (WT) retina, 26.7% (4 out of 15) pseudo-R^2 in linear-Gaussian-GLM model with offset predicts the spike count well under a focused image, compared to 13.3% (2 out of 15) under a +10 D defocused image; 6.6% (1 out of 15) under a +20 D defocused image; 26.7% (4 out of 15) under a −10 D defocused image; 26.7% (4 out of 15) under a −20 D defocused image. There was no significant difference between focused and defocused images. **B**: In LIM retinas, 60% (9 out of 15) pseudo-R^2 in linear-Gaussian-GLM model with offset to predict the spike count under a focused image, compared to 26.7% (4 out of 15) under −10 D defocused image; 13.3% (2 out of 15) under a −20 D defocused image. **C:** Summary of normalized pseudo-R^2 in normal and LIM retinas. Star indicated a significant difference (*t*-test, $p < 0.05$). X axis: Diopters; Y axis: Normalization of the pseudo-R^2.

spike-history and other covariates, including the responses from other neurons (Kelly et al., 2010; Pillow et al., 2008; Truccolo et al., 2005).

"Linear-Gaussian" GLM:

$$Y \left| X, \vec{k} \sim N\left(X\vec{k}, \sigma^2 I\right)\right.$$
$$\hat{k} = \left(X^T X\right)^{-1} X^T Y$$

Poisson GLM:

$$yt|\vec{x}t, \vec{k} \sim \text{Poiss}(\Delta\,\lambda t)\hat{k}$$
$$L = Y^T \log f\left(X\vec{k} - 1^T f\left(X\vec{k}\right)\right)$$

Y is spike, x is stimulus, $\vec{k}$ is linear filter, σ^2 is variance, $\vec{x}$t is vector stimulus at time t; For the response at time t with the linear filter: yt = $\vec{k}\cdot\vec{x}$ t + noise.

Δ λt is Time bin size; f(xt $\vec{k}$) is the nonlinearity probability of spike at bin t.

For all model fits and simulations, the bin time was set as 1 ms. Spike-history dependence was captured by a post-spike filter. The spike history filter was parameterized using raised cosine basis functions. To explore how the timescale of the spike history affected adaptation in the GLM, each model was fitted using only the first i cosine basis functions for each i = 0 to i = N. Thus, N + 1 nested model fits were obtained across a range of spike history lengths. When stated, the length of the spike history filter denotes the time of the peak of the ith basis function. The GLM model was implemented using code from Pillow lab (Pillow et al., 2008) and fitted in MATLAB (ver. R2021a).

2.10. Evaluating model performance

The pseudo-R^2 measures the fraction of explainable log-likelihood captured by the GLM. GLM predictive performance was evaluated using the pseudo-R^2 score (Cameron and Windmeijer, 1997). The pseudo-R^2 score can be applied to Poisson process observations instead of trial-averaged firing rates as required by the standard R^2 measure of explained variance (Benjamin et al., 2018).

The Akaike information criterion (AIC) is a method for model comparison that uses the maximum likelihood, penalized by the number of parameters. AIC is used to compare the fitness of an exponential nonlinearity GLM model (exp-GLM) and a nonparametric estimate of the nonlinearity GLM model (np-GLM). The np- GLM assumes a GLM with an exponential nonlinearity, but makes a "nonparametric" estimate of the nonlinearity.

3. Results

3.1. Lens-induced myopic (LIM) mouse models

Retinoscopy results showed that after 35 days (d) of LIM commencing at day 21, the refractive errors of the treated eyes and untreated control eyes were −3.7 ± 0.7 D and +7.4 ± 0.5 D (mean ± SEM, $P < 0.05$, n = 8), respectively (Fig. 1C).

AL measurements from the corneal surface to the retinal pigment epithelium (RPE) layer corroborated the underlying alterations in the refractive state of the mice's eyes. The AL of the LIM eyes was 3.65 ± 0.12 (mean ± SEM) mm, in contrast to 3.36 ± 0.03 mm ($p < 0.05$, n = 8) (Fig. 1D) of the contra-lateral untreated eyes. The LIM eyes showed an average increase in AL of 0.29 ± 0.03 mm.

3.2. The biophysical properties of RGCs in normal and myopic retinas

As part of the initial experiments, the responses of ON and OFF αRGCs were tested in the retinas of normal and LIM mice under focused and defocused image stimuli. A focused 125 μm diameter with a spatial frequency of 0.0067 cycles/degree image, defined as 0 diopters, was projected onto the outer segment of the photoreceptors. Images defocused by ±10 and ± 20 diopters (D) to simulate myopic vision were then projected through the microscope onto the various layers of the retina. It is possible that the ON and OFF αRGCs tested may not be the cell types that detect the focused/defocused plane in the retina. Nevertheless, the defocused images projected onto these αRGCs would still alter the light intensities and image size, resulting in a blurred edge. The EPSCs of ON and OFF αRGCs were recorded as the first step (Fig. 2). The results of the normal and LIM mice, which served as models of an intact retinal circuit, were then compared with those of Cx36 KO mice, which served as models of a retinal circuit with deficits.

Preliminary experiments were performed on the whole cell level to investigate whether the biophysical properties of ON and OFF αRGCs differed among normal, LIM, and Cx36 KO mice. Based on the calculation, a 5 μm defocus should create a refractive error equal to plus or minus one diopter (Schaeffel, 2008). The light intensities varied from 3.74 x10^4 Rh*/rod/sec to 3.85 x10^4 Rh*/rod/sec. Since certain ON and OFF αRGCs may exhibit varying responses to the focused/defocused images (Pan, 2019), the kinetics of light-evoked EPSCs of ON and OFF αRGCs in normal and LIM retinas were analyzed (Supplemental Fig. 2). To compare the biophysical properties of light-evoked EPSCs between normal and LIM retinas, nine aspects of the EPSCs' properties were measured: area, time to maximum rise (decay), maximum rise (decay) slope, and 80%–20% rise (decay) time and slope. Each RGC was

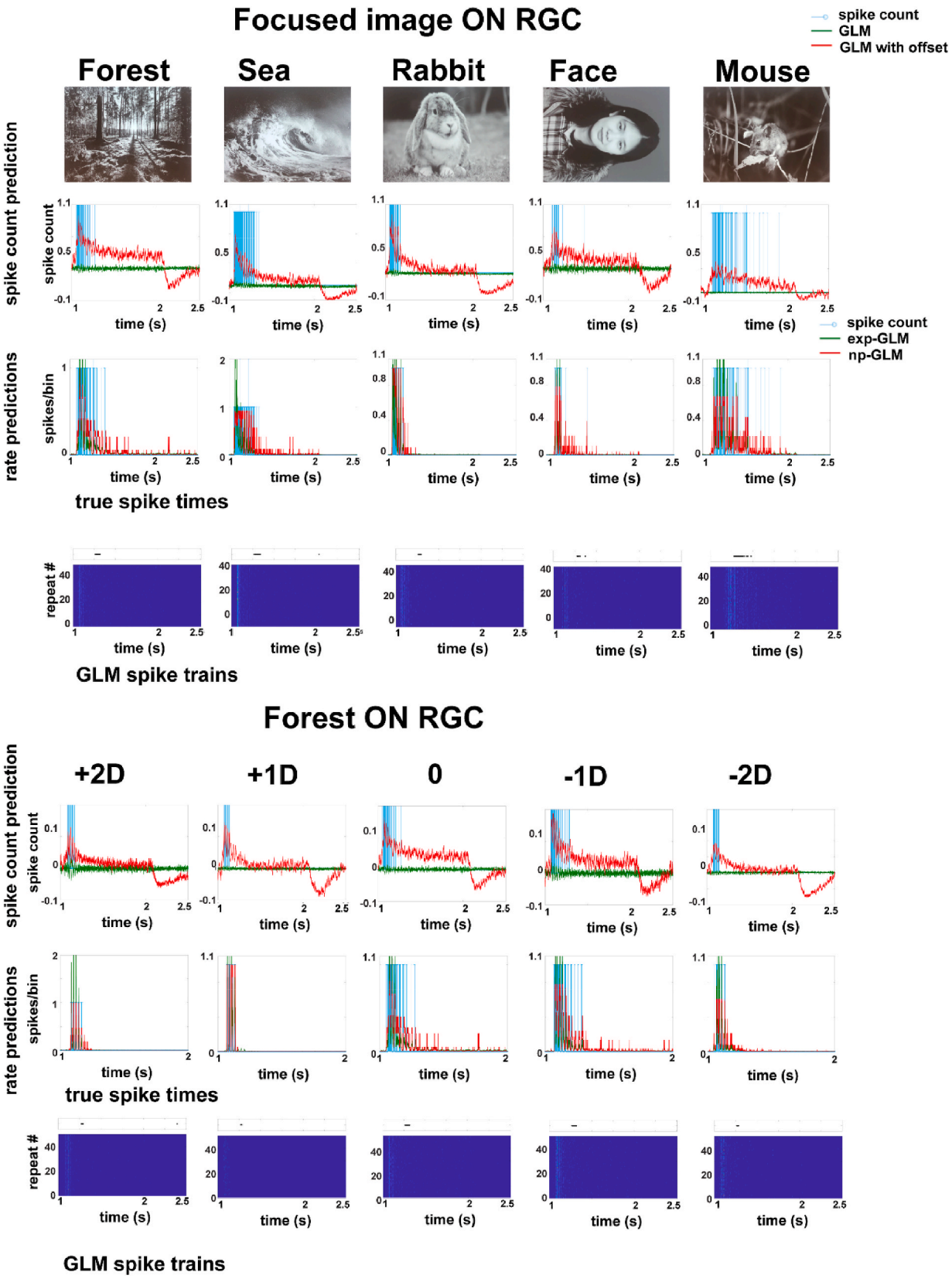

Fig. 7. GLM models predict natural scenes stimuli on ON RGC in normal retinas. The figures show GLM models applied to predict the spike count (upper row), rate (middle row), true spike times and spike trains (lower row) under different focused natural scene projections. The natural scenes are forest, sea, rabbit, face, and mouse from left to right. GLM models predict the spike count (upper row), rate (middle row), true spike times and spike trains (lower row) of the forest image well under focused, ±1 diopter, and ±2 diopters defocused projection.

recorded under focused, ±10 D and ±20 D defocused images to capture these general properties of EPSCs. Then, the maximal responses of these different aspects of EPSCs were normalized. These nine characteristics of EPSCs were selected due to their ability to show the physical characteristics of the cells, and it was anticipated that the reactions to focused and defocused stimuli would be distinct. According to our previous results, the response to a focused image is hypothesized to be either maximal or minimal, as it may have a better signal-to-noise ratio than a defocused image (Pan, 2019).

In both normal and LIM retinas, the ON/OFF αRGCs with either maximal or minimal responses in the nine biophysical measurements were counted under focused image stimulation. Out of these nine biophysical properties, 89% of ON/OFF αRGCs in the normal retina, with the exception of the time of max decay slope for ON αRGCs and the max decay slope for OFF αRGCs, had either maximal or minimal responses. Six of the eight biophysical measurements in ON/OFF αRGCs in the normal retina showed a significant difference between focused and at least one of the defocused images (*t*-test, $p < 0.05$). In comparison, all nine biophysical measurements of the ON and OFF αRGCs in the LIM retina had either maximal or minimal responses for both focused and defocused images. Six of the nine measurements showed a significant difference between focused and other defocused images (*t*-test, $p < 0.05$).

Among 12 ON/OFF αRGCs from normal retinas, two-thirds of measurements recorded maximal or minimal responses, respectively. Similarly, two-thirds of measurements were observed in 39 ON αRGCs, although the response was slightly lower (56%) in 57 OFF αRGCs of myopic (LIM) retinas. The kinetics of EPSCs revealed that a single RGC from either normal or LIM retinas could reflect different focus/defocus images projection. However, biophysical responses to focused and defocused images did not significantly differ between the LIM and the normal retinas.

Most RGCs in the mouse retina require Cx36 for their functioning, so the absence of Cx36 would likely lead to the loss of heterozygous coupling between αRGCs and amacrine cells. This could significantly impact the functioning of the retinal circuitry (Farajian et al., 2011; Pan et al., 2010). Testing of the biophysical properties of whole-cell responses in ON and OFF αRGCs of Cx36 KO mouse retinas revealed that only 22% (2 out of 9) of measurements in the ON αRGCs and 11% (1 out of 9) of measurements in the OFF αRGCs resulted in a maximal or minimal response (Supplemental Fig. 3). Further analysis of the ON/OFF αRGCs in Cx36 KO retinas revealed no difference in these nine biophysical properties, indicating no difference in response to focused and defocused images. Comparatively, 16.7% of measurements in 10 ON αRGCs and 8.6% in 9 OFF αRGCs had either maximal or minimal responses in Cx36 KO mice. This was a significant difference compared to the responses observed in normal and LIM retinas, and suggests that either the complete retinal circuit or amacrine cells coupled with RGCs may play a role in the αRGC response to focused and defocused images.

Even though these nine features of EPSCs highlighted the distinction between Cx36 KO and normal retinas, it could be argued that the biophysical properties chosen were random, and thus, further research is needed.

3.3. Computation of the GLM model for encoding focused/defocused images to RGCs in normal and myopic retinas

In the next step, Poisson GLMs (Fig. 3) were used for qualitative dynamical and quantitative statistical analysis of single-neuron response properties in LIM and normal retinas. The stimulus filter calculates the spatio-temporal integration of light in the outer retina and passive dendritic filtering; the post-spike filter mimics voltage-activated currents following a spike, and the coupling filters represent synaptic or electrical interactions between cells. The exponential nonlinearity then implements a 'soft threshold', converting membrane potential to instantaneous spike probability. These post-spike and coupling filters, which allow stochastic spiking in one cell to affect subsequent population activity, give rise to shared, non-Poisson variability in the model response. It is known that αRGCs include different subtypes, each with distinct physiological and morphological features. These subtypes also have different response dynamics, such as sustained or transient (Krieger et al., 2017). The GLM model was used to estimate the differences in the encoding performance across αRGCs subtypes. The spike count of ON and OFF αRGCs in normal retinas (Fig. 4) was recorded and predicted using a linear-Gaussian GLM. The stimulus was normalized, and the training perfect of pseudo-R^2 measures was used to evaluate and compare the performance of the linear-Gaussian GLM model with and without offset. The results showed that the spike counts were better fitted with the offset. Additionally, the use of an offset also improved the fit of the spike counts of αRGCs from LIM retinas with a linear-Gaussian-GLM model with offset (Fig. 5). The pseudo-R^2 of linear-Gaussian-GLM model with offset was 0.1 in the focused image for normal cells, and ranged from 0.035 ± 0.02 (mean ± SEM) with defocused images (±10D and ±20D) in ON αRGCs, compared to 0 of pseudo-R^2 in a linear-Gaussian-GLM model without offset. The pseudo-R^2 of the linear-Gaussian-GLM model with offset was 0.58 in the focused image, and ranged from 0.47 ± 0.06 with defocused images (±10D and ±20D) in the OFF αRGCs, compared to 0 of pseudo-R^2 in linear-Gaussian-GLM model without offset.

For LIM retinas, the pseudo-R^2 of linear-Gaussian-GLM model with offset was also 0.1 in the focused image, but ranged from 0.028 ± 0.08 (mean ± SEM) with defocused images (±10D and ±20D) in the ON αRGCs, compared to 0 without offset. The pseudo-R^2 of linear-Gaussian GLM model with offset was 0.05 in the focused image, and ranged from 0.02 ± 0.01 with defocused images (±10D and ±20D) in the OFF αRGCs. The spike count of the ON and OFF αRGCs of both normal and LIM retinas was a better fit when using the linear-Gaussian-GLM model with an offset. Therefore, the linear-Gaussian-GLM model with an offset better fits the spike counts of ON and OFF αRGCs in both normal and LIM retinas.

AIC comparison of fitting of the rate prediction with the exponential nonlinearity GLM model (exp-GLM) and nonparametric estimate of the nonlinearity GLM model (np-GLM), plotted by units of spikes/bin, indicated that np-GLM predicted spike rate was better for both focused and defocused images. As shown in Fig. 4, the AIC difference between exp-GLM and np-GLM is 201 (the ON αRGCs) and 1764 (the OFF αRGCs) for the focused image, demonstrating the superiority of the np-GLM fitting. Similarly, the np-GLM fitting was superior for defocused images (±10D and ±20D) in both ON and OFF αRGCs. The rate prediction in 13 out of 15 (87%) ON and OFF αRGCs in normal retinas were better fitted with np-GLM, while only 2 out of 15 (13%) ON and OFF αRGCs in normal retinas had better fitted with exp-GLM under +20D defocused images (Supplemental Fig. 4). Compared to the focused image and other defocused images, +20D defocused image projected the blurriest images on the inner retina. This could explain why some subtype αRGCs might recruit different amacrine cells to encode the visual information, which could explain the difference in exp-GLM and np-GLM fitting in some RGCs.

As with normal retinas, the rate prediction was better fitted with the nonlinearity GLM model (np-GLM) estimate, with AIC indicating that the np-GLM prediction rate was better in focused/defocused images in LIM retinas (Fig. 5). This was supported by the AIC difference between exp-GLM and np-GLM: 323 (for the ON αRGCs) and 426 (for the OFF αRGCs) under focused images. Two-thirds (10 out of 15, 66.7%) of ON and OFF αRGCs in LIM retinas showed a better fit with np-GLM, while the remaining five ON and OFF αRGCs had a better fit by exp-GLM (33.3%) under −10D and −20D defocused images separately (as shown in Supplemental Fig. 4). This indicated that αRGCs had different coding performances under defocused images in LIM retinas.

In summary, the spike count of ON and OFF αRGCs in normal (WT) and LIM retinas was better fitted by the linear-Gaussian-GLM model with offset. The rate prediction of 87% in ON and OFF αRGCs in normal

retinas compared to 67% in LIM was a better fit with np-GLM.

The raster plot displayed the spiking activity of αRGCs over time in response to the stimuli. As predicted by GLM, both ON and OFF αRGCs in normal retinas had raster plots of their spike trains under focused/defocused images. Compared to the defocused images, especially those under ±20D, the spike trains under the focused image had a clear response (11 out of 15 ON and OFF αRGCs, 4 uncertain) in the raster plot (as shown in Supplemental Figs. 5A and B). The raster plot allows inspection of the neural activity over time, which may indicate that αRGCs had different spiking activities under focused/defocused image stimuli in the normal retinas.

Raster plots of spike train predicted by GLM showed that the focused image had a relatively clear response (8 out of 12 OFF αRGCs, 4 uncertain) compared to the ±20D image stimuli in the OFF αRGCs of LIM retinas (Supplemental Fig. 5D). Compared to the WT retina, ON αRGCs had a relatively clear response under focused images, but not under ±20D defocused image in LIM retinas (8 out of 15 αRGCs, 7 uncertain, Supplemental Fig. 5C). This phenomenon may be explained by potential amendment and plasticity in the myopic retinal circuit, but further investigation is required.

The following study investigated whether the pseudo-R^2 in linear-Gaussian-GLM model with offset to predict the spike count could be used to compare the fitting of focused and defocused images. If so, the results showed that focused images could be better encoded in the retina than blurred (defocused) images. If not, the retina would faithfully encode the images projected on the retina. The pseudo-R^2 of focused and defocused images (±10D and ±20D) were normalized by maximal number and then compared. In normal retina, 26.7% (4 out of 15) of the pseudo-R^2 in linear-Gaussian-GLM model with offset predicted the spike count well under focused images, compared to 13.3% (2 out of 15) under +10D defocused image, 6.6% (1 out of 15) under +20D, 26.7% (4 out of 15) under −10 D, and 26.7% (4 out of 15) under −20 D defocused images (Fig. 6A showed the normalized pseudo-R^2). There was no significant difference in the ability to predict the spike count in normal retinas between focused and defocused images. However, the linear-Gaussian GLM model with offset was more effective at predicting the spike count in LIM retinas, with 60% (9 of 15) accuracy for focused images and 26.7% (4 out of 15) and 13.3% (2 of 15) accuracy for −10 D and −20 D defocused image, respectively (Fig. 6B showed the normalized the pseudo-R^2). These results suggest that focused images were better coded with the linear-Gaussian GLM model with offset in the LIM retina (Fig. 6C). This difference in the ability to predict the spike between the normal and LIM retinas likely reflected the amendment in visual processing or the plasticity in the retinal circuit of the LIM retinas.

3.4. RGC responses to natural scene stimuli in the normal retina

To evaluate the response of single RGC in normal retina to various natural scenes, including a forest, the sea, a rabbit, a face, and a mouse, which varied in shape, contrast, and brightness, the pseudo-R^2 of the linear-Gaussian GLM model with offset was measured. To test whether single RGC coding can be accurately identified by a GLM model, only normal retinal cells were used for the experiment.

When testing the spike count in natural scenes with a linear-Gaussian GLM model with an offset, the pseudo-R^2 value varied between scenes, with 0.01 for the forest, 0.14 for the sea, 0.04 for the rabbit, 0.1 for the face, and 0.01 for the mouse. AIC results indicated that np-GLM was better than the exp-GLM at predicting the rate. As expected, the true spike times and spike trains were different when natural images were used.

For example, the pseudo-R^2 of the linear-Gaussian GLM model with an offset for predicting the spike count in the focused forest image was 0.01. However, pseudo-R^2 could not be calculated for ±1 D and ±2 D defocused images of the forest (Fig. 7). Only up to ±2 D defocused images were used, as the images were similar if a more than ±3 D defocused image was generated. The np-GLM was better at predicting the rate for the focused forest image, but exp-GLM was better suited for predicting ±1 D and ±2 D defocused forest images. The raster plots of spike trains predicted by GLM also showed that the focused forest image had a distinct response.

4. Discussion

Despite the increasing prevalence of myopia worldwide, there are no effective methods to prevent or reverse its progression, largely due to the lack of a clear understanding of the underlying mechanism. A key question is whether the RGCs in the myopic retina process visual information differently than those in the normal retina, which could help identify the entity(ies) responsible for myopia. To answer this question, the coding performance of RGCs predicted by the GLM model was compared between the retinas of LIM and normal (WT) mice.

Knowledge of how RGCs encode the features of a particular visual stimulus can provide insight into how visual information is transmitted in the retina (Field and Chichilnisky, 2007; Gollisch and Meister, 2010). More than 40 RGC subtypes in the mouse retinas extract complex features of specific visual information and exhibit specific temporal response properties to image stimuli. These coding properties of RGC are known to be shaped by their circuits, particularly coupled amacrine cells (Kaplan and Shapley, 1986; Roska and Werblin, 2001). The mouse retina contains four distinct functional subtypes of αRGCs (ON-sustained, ON-transient, OFF-sustained, and OFF-transient) (Krieger et al., 2017). In the retina, the responses of ON and OFF αRGCs originate from stimulation of the outer retina, especially between photoreceptor-to-bipolar cell synapses (Masland, 2012). Unlike focused images, defocused images projected on the retina have a broader area with blurred edges and different light intensities, which could lead to different responses from αRGCs (Pan, 2019). Although αRGCs may not be the cells that sense the focused/defocused plane in the retina, the coding performance of ON and OFF αRGCs with transient and sustained subtypes was investigated between normal and myopic retinas in this study.

Previous studies have analyzed the responses of αRGCs to focused and defocused images, as well as their firing patterns in larger neural populations (Banerjee et al., 2020). This study explored the impact of the myopic retina on the encoding of visual stimuli. A model-based methodology was used, with a GLM model (Paninski, 2004; Plesser and Gerstner, 2000; Truccolo et al., 2005) applied to describe the encoding of stimuli in the spike trains of αRGCs. Although this model is phenomenological, its components can be compared to biophysical mechanisms (Pillow et al., 2008). White noise applied in receptive field analysis is a common way to describe neural stimulus selectivity in a population of neurons; however, in this study, GLM was able to predict the difference in αRGCs encoding of focused and defocused images. The pseudo-R^2 in linear-Gaussian-GLM model showed the difference in encoding between ON and OFF αRGCs. The variation in coupling patterns between ON and OFF αRGCs may cause the difference: ON αRGCs are coupled only with amacrine cells in the mouse retina, while OFF αRGCs are coupled with the same OFF αRGCs and amacrine cells (Pan et al., 2010; Volgyi et al., 2009). The difference in coupling patterns between ON and OFF αRGCs may affect the encoding performance.

Neural computations in the retina require complex and intact circuits (Demb and Singer, 2015). There is concern about whether the GLM model can be applied to analyze different subtypes of αRGCs in the same way. However, based on a normal and intact circuit, the GLM model can be applied to predict the responses of subtypes of αRGCs to visual stimuli (Chichilnisky, 2001; Pillow et al., 2005; Shapley, 2009). If the myopic retina encodes visual information differently from the normal retina, then the predicted results from GLM model would reflect these differences. The difference between normal and myopic retina was expected to be small. Recordings from populations of ON and OFF αRGCs with focused/defocused images were fitted to the GLM model. The model contained many parameters that specified the shapes of all filters, and they were fitted by maximizing the likelihood. The GLM models were

then used to predict the spike counts of natural scenes, as well as rate, true spike times, and spike trains. Natural scenes were found to induce different spike trains. The linear-Gaussian GLM model best predicted the spike counts with offset in both normal and LIM retinas. There was no difference in performance between focused and defocused images when using the pseudo-R^2 in linear-Gaussian GLM model with offset to predict the spike count in the normal retinas. However, the pseudo-R^2 in linear-Gaussian GLM model with offset was better for predicting the spike count under a focused image than the defocused image in LIM retinas. This difference may reflect the amendment in encoding focused and defocused images between normal and LIM retinas. Regarding the spike rate, AIC indicated that np-GLM predicted focused and defocused images better in both LIM and normal retinas. However, when a +20D defocused image with the blurriest edge was projected on the inner retina, the exp-GLM model fitted better in some subtype αRGCs in normal retinas. These αRGCs may recruit different subtypes or amounts of amacrine cells to encode the visual signalling. AIC cannot be used to compare the fitting quantitively. There was a difference in predicting the spike rate by np-GLM between LIM and normal retinas. Around 33% of αRGCs in LIM retinas were better fit by exp-GLM under −10D and −20D defocused images compared to only 13% of αRGCs in normal retinas. These results indicated the difference in the myopic retina's encoding performance under defocused images. The defocused status of the LIM myopic retinas may induce plasticity of the retinal circuit to adapt to the myopic status. Studies of this group have previously demonstrated that in the form-deprived myopic mouse retina, phosphorylation of Cx36 increased in myopic retinas, which may be an adaptation to code for defocused images (Banerjee et al., 2021; Banerjee et al., 2020).

To understand how RGCs process visual information in normal and myopic retinas, artificial stimuli that can be precisely controlled and manipulated were applied. However, this approach has limitations in that it does not reflect the complexity and diversity of the natural visual environment. To address this limitation, we used natural scenes as stimuli to provide a more realistic way to study RGC responses in the retina. Natural scenes are complex, and they exhibit a wide range of spatial and temporal frequencies, contrast levels, and color variations (though color was not studied in this research). By using natural scenes, we were able to observe how RGCs respond to different features of the visual scene and to reveal the underlying mechanisms of visual processing in the retina. Single RGCs in the normal retina can accurately encode various natural scenes. In addition to natural scenes, we projected both focused and blurred images (blurred but still in focus) onto the retina to study the response of RGCs. We found that the RGC responses to natural scenes were similar to those observed with the use of artificial stimuli.

From the perspective of the real response of αRGCs, more than two-thirds of their EPSCs biophysical properties in terms of area, time of maximal rise (decay) slope, maximal rise (decay) slope, 80%–20% rise (decay) time, and slope had either maximal or minimal responses to focused images in both normal and LIM retinas. The results indicated that normal and myopic retinas can faithfully encode focused and defocused images. Single RGC in both LIM and normal retinas have similar biophysical responses to focused and defocused images.

Cx36 KO mice were used as a control to confirm the importance of intact retinal circuits in encoding focused and defocused images by αRGCs. In the Cx36 KO mice, the outer and inner retinas were affected, with loss of secondary and tertiary rod pathways in the outer retina and AC couplings with RGCs (Bloomfield and Volgyi, 2009). αRGCs lost their maximal or minimal responses to focused images in more than 78% of the biophysical properties compared to normal and LIM retinas. This may be due to the disappearance of most amacrine cells coupled to RGCs in Cx36 KO mice (Pan et al., 2010). Defocused images have blurred edges, different focused planes, and varied light intensities compared with focused images. Amacrine cells may provide feedback inhibition, surround inhibition, adaptation, signal averaging, and noise reduction (Olveczky et al., 2003) to the signaling from RGCs, suggesting that they may take part in encoding focused/defocused images. As a control, Cx36 KO mice lose the filters in the outer and inner retina. Moreover, evidence from human studies suggests that GJD2, the gene encoding for the Cx36 protein, which has a high degree of SNPs across the human population, appears to be important in myopia development. Cx36 is considered as a potential modulator of myopia development in both human and animal models (Quint et al., 2021; Verhoeven et al., 2013). Further studies are needed to create LIM Cx36 KO mice to ascertain if Cx36-involving neural circuits factor significantly in myopia development. For example, by comparing experiments in encoding performance using WT and LIM mice with Cx36 KO and LIM Cx36 KO mice, we might determine the hypothetical influence of Cx36-mediated electrical coupling on myopia development.

It has been hypothesized that the myopic retina may adapt to defocused images, and that the retinal circuit could be altered if the defocused status were to remain. The changed entities in the retinal circuit could be used as a potential therapeutic approach for myopia control. However, once the retinal circuit had adapted to the long-term myopic retina, the cascade triggered by the myopic status may have already impacted the axial length. This may explain why myopia continues progressing even after the ametropia status has been corrected.

5. Conclusion

GLM model was used to determine the encoding of focused/defocused images by ON and OFF αRGCs in both myopic and normal retinas. The intact retinal circuit involving Cx36 was found to be critical in computing the difference in visual signaling between focused/defocused images. The different performances of GLM model with offset in LIM retinas suggested the possible amendment and plasticity of the retina circuit in myopic retinas.

6. Limitations of the study

Myopic marmoset or other monkey models may be more suitable than the myopic mouse model with a retinal macular or fovea-like structure. In this study, the LIM mouse model was observed and recorded only at one-time point, following three weeks of lens treatment in an 8-week-old mouse. More research is necessary to study long-term LIM models, as adaptations in the retinal circuit may take time to manifest.

Funding

This study was supported by The Hong Kong Polytechnic University grant: UAG4, UAHA, UALC, UAQC and University Research Facility in Behavioral and Systems Neuroscience. This study was also supported by the Hong Kong Research Grants Council (ECS/RGC; 25103918 (FP); 15106018 (DT), Hong Kong, SAR); InnoHK initiative and the Hong Kong Special Administrative Region Government. "百城百园" 专项启动基金" (I2021A010); 深圳市基础研究（面上项目） (Shenzhen Municipal Science and Technology Innovation Commission, JCYJ20210324130809025).

Author contributions

QW, CH.S., BZ, SB, CT.Q., TZ, MY.C, DYT, FP: Acquisition, analysis, and interpretation of data. FP conception and design of the work; FP: drafting the article. The authors read and approved the final manuscript.

Declaration of competing interest

The authors declare no competing financial interests.

Data availability

Data will be made available on request.

Acknowledgments

We are grateful to Dr. Maureen Boost for the critical reading of the manuscript. We thank Dr. Ka Fai Kevin Wong and the Industrial Center of the Hong Kong Polytechnic University for their assistance with patterned light stimuli and Matlab software in machine learning.

Appendix A. Supplementary data

Supplementary data to this article can be found online at https://doi.org/10.1016/j.exer.2023.109616.

References

Baird, P.N., Saw, S.M., Lanca, C., Guggenheim, J.A., Smith Iii, E.L., Zhou, X., Matsui, K. O., Wu, P.C., Sankaridurg, P., Chia, A., Rosman, M., Lamoureux, E.L., Man, R., He, M., 2020. Myopia. Nat. Rev. Dis. Prim. 6 (1), 99. https://doi.org/10.1038/s41572-020-00231-4.

Banerjee, S., Wang, Q., So, C.H., Pan, F., 2020a. Defocused images change multineuronal firing patterns in the mouse retina. Cells 9 (3), E530. https://doi.org/10.3390/cells9030530.

Banerjee, S., Wang, Q., Tang, G., So, C., Shan, S.W., Li, K.K., Do, C.W., Pan, F., 2021. Functional connexin35 increased in the myopic chicken retina. Vis. Neurosci. 38, E008. https://doi.org/10.1017/S0952523821000079.

Banerjee, S., Wang, Q., Zhao, F., Tang, G., So, C., Tse, D., To, C.H., Feng, Y., Zhou, X., Pan, F., 2020b. Increased Connexin36 phosphorylation in AII amacrine cell coupling of the mouse myopic retina. Front. Cell. Neurosci. 14, 124. https://doi.org/10.3389/fncel.2020.00124.

Benjamin, A.S., Fernandes, H.L., Tomlinson, T., Ramkumar, P., VerSteeg, C., Chowdhury, R.H., Miller, L.E., Kording, K.P., 2018. Modern machine learning as a benchmark for fitting neural responses. Front. Comput. Neurosci. 12, 56. https://doi.org/10.3389/fncom.2018.00056.

Bloomfield, S.A., Miller, R.F., 1982. A physiological and morphological study of the horizontal cell types of the rabbit retina. J. Comp. Neurol. 208 (3), 288–303. https://doi.org/10.1002/cne.902080306.

Bloomfield, S.A., Volgyi, B., 2004. Function and plasticity of homologous coupling between AII amacrine cells. Vis. Res. 44 (28), 3297–3306. https://doi.org/10.1016/j.visres.2004.07.012.

Bloomfield, S.A., Volgyi, B., 2009. The diverse functional roles and regulation of neuronal gap junctions in the retina. Nat. Rev. Neurosci. 10 (7), 495–506. https://doi.org/10.1038/nrn2636.

Borghuis, B.G., Marvin, J.S., Looger, L.L., Demb, J.B., 2013. Two-photon imaging of nonlinear glutamate release dynamics at bipolar cell synapses in the mouse retina. J. Neurosci. 33 (27), 10972–10985. https://doi.org/10.1523/JNEUROSCI.1241-13.2013.

Botella-Soler, V., Deny, S., Martius, G., Marre, O., Tkacik, G., 2018. Nonlinear decoding of a complex movie from the mammalian retina. PLoS Comput. Biol. 14 (5), e1006057 https://doi.org/10.1371/journal.pcbi.1006057.

Cameron, A.C., Windmeijer, F.A.G., 1997. An R-squared measure of goodness of fit for some common nonlinear regression models. J. Econom. 77 (2), 329–342. <Go to ISI>://WOS:A1997WK30400003.

Chichilnisky, E.J., 2001. A simple white noise analysis of neuronal light responses. Network 12 (2), 199–213. https://www.ncbi.nlm.nih.gov/pubmed/11405422.

Crapper, D.R., Noell, W.K., 1963. Retinal excitation and inhibition from direct electrical stimulation. J. Neurophysiol. 26, 924–947. https://doi.org/10.1152/jn.1963.26.6.924.

Demb, J.B., Singer, J.H., 2015. Functional circuitry of the retina. Annu Rev Vis Sci 1, 263–289. https://doi.org/10.1146/annurev-vision-082114-035334.

Duan, X., Qiao, M., Bei, F., Kim, I.J., He, Z., Sanes, J.R., 2015. Subtype-specific regeneration of retinal ganglion cells following axotomy: effects of osteopontin and mTOR signaling. Neuron 85 (6), 1244–1256. https://doi.org/10.1016/j.neuron.2015.02.017.

El Hady, A., 2016. Closed Loop Neuroscience.

Farajian, R., Pan, F., Akopian, A., Volgyi, B., Bloomfield, S.A., 2011. Masked excitatory crosstalk between the ON and OFF visual pathways in the mammalian retina. J. Physiol. 589 (Pt 18), 4473–4489. https://doi.org/10.1113/jphysiol.2011.213371.

Field, G.D., Chichilnisky, E.J., 2007. Information processing in the primate retina: circuitry and coding. Annu. Rev. Neurosci. 30, 1–30. https://doi.org/10.1146/annurev.neuro.30.051606.094252.

Foster, P.J., Jiang, Y., 2014. Epidemiology of myopia. Eye (Lond) 28 (2), 202–208. https://doi.org/10.1038/eye.2013.280.

Gollisch, T., 2009. Throwing a glance at the neural code: rapid information transmission in the visual system. HFSP J. 3 (1), 36–46. https://doi.org/10.2976/1.3027089.

Gollisch, T., Meister, M., 2010. Eye smarter than scientists believed: neural computations in circuits of the retina. Neuron 65 (2), 150–164. https://doi.org/10.1016/j.neuron.2009.12.009.

Granit, R., 1946. The distribution of excitation and inhibition in single-fibre responses from a polarized retina. J. Physiol. 105, 45–53. https://www.ncbi.nlm.nih.gov/pubmed/20994070.

Gutig, R., Gollisch, T., Sompolinsky, H., Meister, M., 2013. Computing complex visual features with retinal spike times. PLoS One 8 (1), e53063. https://doi.org/10.1371/journal.pone.0053063.

Holden, B.A., Fricke, T.R., Wilson, D.A., Jong, M., Naidoo, K.S., Sankaridurg, P., Wong, T.Y., Naduvilath, T.J., Resnikoff, S., 2016. Global prevalence of myopia and high myopia and temporal trends from 2000 through 2050. Ophthalmology 123 (5), 1036–1042. https://doi.org/10.1016/j.ophtha.2016.01.006.

Hubel, D.H., Wiesel, T.N., 1968. Receptive fields and functional architecture of monkey striate cortex. J. Physiol. 195 (1), 215–243. https://doi.org/10.1113/jphysiol.1968.sp008455.

Jiang, X., Kurihara, T., Kunimi, H., Miyauchi, M., Ikeda, S.I., Mori, K., Tsubota, K., Torii, H., Tsubota, K., 2018. A highly efficient murine model of experimental myopia. Sci. Rep. 8 (1), 2026. https://doi.org/10.1038/s41598-018-20272-w.

Kaplan, E., Shapley, R.M., 1986. The primate retina contains two types of ganglion cells, with high and low contrast sensitivity. Proc. Natl. Acad. Sci. U.S.A. 83 (8), 2755–2757. https://doi.org/10.1073/pnas.83.8.2755.

Kelly, R.C., Smith, M.A., Kass, R.E., Lee, T.S., 2010. Local field potentials indicate network state and account for neuronal response variability. J. Comput. Neurosci. 29 (3), 567–579. https://doi.org/10.1007/s10827-009-0208-9.

Krieger, B., Qiao, M., Rousso, D.L., Sanes, J.R., Meister, M., 2017. Four alpha ganglion cell types in mouse retina: function, structure, and molecular signatures. PLoS One 12 (7), e0180091. https://doi.org/10.1371/journal.pone.0180091.

Leonardo, A., Meister, M., 2013. Nonlinear dynamics support a linear population code in a retinal target-tracking circuit. J. Neurosci. 33 (43), 16971–16982. https://doi.org/10.1523/JNEUROSCI.2257-13.2013.

Masland, R.H., 2012. The neuronal organization of the retina. Neuron 76 (2), 266–280. https://doi.org/10.1016/j.neuron.2012.10.002.

Olveczky, B.P., Baccus, S.A., Meister, M., 2003. Segregation of object and background motion in the retina. Nature 423 (6938), 401–408. https://doi.org/10.1038/nature01652.

Pan, F., 2019. Defocused image changes signaling of ganglion cells in the mouse retina. Cells 8 (7), E640. https://doi.org/10.3390/cells8070640.

Pan, F., Massey, S.C., 2007. Rod and cone input to horizontal cells in the rabbit retina. J. Comp. Neurol. 500 (5), 815–831. https://doi.org/10.1002/cne.21127.

Pan, F., Paul, D.L., Bloomfield, S.A., Volgyi, B., 2010. Connexin36 is required for gap junctional coupling of most ganglion cell subtypes in the mouse retina. J. Comp. Neurol. 518 (6), 911–927. https://doi.org/10.1002/cne.22254.

Pan, F., Toychiev, A., Zhang, Y., Atlasz, T., Ramakrishnan, H., Roy, K., Volgyi, B., Akopian, A., Bloomfield, S.A., 2016. Inhibitory masking controls the threshold sensitivity of retinal ganglion cells. J. Physiol. 594 (22), 6679–6699. https://doi.org/10.1113/JP272267.

Paninski, L., 2004. Maximum likelihood estimation of cascade point-process neural encoding models. Network 15 (4), 243–262. https://www.ncbi.nlm.nih.gov/pubmed/15600233.

Peichl, L., 1991. Alpha ganglion cells in mammalian retinae: common properties, species differences, and some comments on other ganglion cells. Vis. Neurosci. 7 (1–2), 155–169. https://doi.org/10.1017/s0952523800011020.

Pillow, J.W., Paninski, L., Uzzell, V.J., Simoncelli, E.P., Chichilnisky, E.J., 2005. Prediction and decoding of retinal ganglion cell responses with a probabilistic spiking model. J. Neurosci. 25 (47), 11003–11013. https://doi.org/10.1523/JNEUROSCI.3305-05.2005.

Pillow, J.W., Shlens, J., Paninski, L., Sher, A., Litke, A.M., Chichilnisky, E.J., Simoncelli, E.P., 2008. Spatio-temporal correlations and visual signalling in a complete neuronal population. Nature 454 (7207), 995–999. https://doi.org/10.1038/nature07140.

Plesser, H.E., Gerstner, W., 2000. Noise in integrate-and-fire neurons: from stochastic input to escape rates. Neural Comput. 12 (2), 367–384. https://doi.org/10.1162/089976600300015835.

Quint, W.H., Tadema, K.C.D., de Vrieze, E., Lukowicz, R.M., Broekman, S., Winkelman, B.H.J., Hoevenaars, M., de Gruiter, H.M., van Wijk, E., Schaeffel, F., Meester-Smoor, M., Miller, A.C., Willemsen, R., Klaver, C.C.W., Iglesias, A.I., 2021. Loss of Gap Junction Delta-2 (GJD2) gene orthologs leads to refractive error in zebrafish. Commun. Biol. 4 (1), 676. https://doi.org/10.1038/s42003-021-02185-z.

Roska, B., Werblin, F., 2001. Vertical interactions across ten parallel, stacked representations in the mammalian retina. Nature 410 (6828), 583–587. https://doi.org/10.1038/35069068.

Schaeffel, F., 2008. Test systems for measuring ocular parameters and visual function in mice. Front. Biosci. 13, 4904–4911. http://www.ncbi.nlm.nih.gov/pubmed/18508555.

Schaeffel, F., Wildsoet, C., 2013. Can the retina alone detect the sign of defocus? Ophthalmic Physiol. Opt. 33 (3), 362–367. https://doi.org/10.1111/opo.12058.

Shapley, R., 2009. Linear and nonlinear systems analysis of the visual system: why does it seem so linear? A review dedicated to the memory of Henk Spekreijse. Vis. Res. 49 (9), 907–921. https://doi.org/10.1016/j.visres.2008.09.026.

Smith 3rd, E.L., Hung, L.F., 1999. The role of optical defocus in regulating refractive development in infant monkeys. Vis. Res. 39 (8), 1415–1435. http://www.ncbi.nlm.nih.gov/pubmed/10343811.

Smith 3rd, E.L., Hung, L.F., Huang, J., Arumugam, B., 2013. Effects of local myopic defocus on refractive development in monkeys. Optom. Vis. Sci. 90 (11), 1176–1186. https://doi.org/10.1097/OPX.0000000000000038.

Troy, J.B., Lee, B.B., 1994. Steady discharges of macaque retinal ganglion cells. Vis. Neurosci. 11 (1), 111–118. https://doi.org/10.1017/s0952523800011159.

Truccolo, W., Eden, U.T., Fellows, M.R., Donoghue, J.P., Brown, E.N., 2005. A point process framework for relating neural spiking activity to spiking history, neural ensemble, and extrinsic covariate effects. J. Neurophysiol. 93 (2), 1074–1089. https://doi.org/10.1152/jn.00697.2004.

Verhoeven, V.J., Hysi, P.G., Wojciechowski, R., Fan, Q., Guggenheim, J.A., Hohn, R., MacGregor, S., Hewitt, A.W., Nag, A., Cheng, C.Y., Yonova-Doing, E., Zhou, X., Ikram, M.K., Buitendijk, G.H., McMahon, G., Kemp, J.P., Pourcain, B.S., Simpson, C.

L., Makela, K.M., Hammond, C.J., 2013. Genome-wide meta-analyses of multiancestry cohorts identify multiple new susceptibility loci for refractive error and myopia. Nat. Genet. 45 (3), 314–318. https://doi.org/10.1038/ng.2554.

Vitale, S., Ellwein, L., Cotch, M.F., Ferris 3rd, F.L., Sperduto, R., 2008. Prevalence of refractive error in the United States, 1999-2004. Arch. Ophthalmol. 126 (8), 1111–1119. https://doi.org/10.1001/archopht.126.8.1111.

Volgyi, B., Chheda, S., Bloomfield, S.A., 2009. Tracer coupling patterns of the ganglion cell subtypes in the mouse retina. J. Comp. Neurol. 512 (5), 664–687. https://doi.org/10.1002/cne.21912.

Volgyi, B., Pan, F., Paul, D.L., Wang, J.T., Huberman, A.D., Bloomfield, S.A., 2013. Gap junctions are essential for generating the correlated spike activity of neighboring retinal ganglion cells. PLoS One 8 (7), e69426. https://doi.org/10.1371/journal.pone.0069426.

Wang, Q., Banerjee, S., So, C., Qiu, C., Lam, H.C., Tse, D., Volgyi, B., Pan, F., 2020. Unmasking inhibition prolongs neuronal function in retinal degeneration mouse model. FASEB J 34 (11), 15282–15299. https://doi.org/10.1096/fj.202001315RR.

Wang, Q., Banerjee, S., So, C., Qiu, C., Sze, Y., Lam, T.C., To, C.H., Pan, F., 2021. The effect of low-dose atropine on alpha ganglion cell signaling in the mouse retina. Front. Cell. Neurosci. 15, 664491 https://doi.org/10.3389/fncel.2021.664491.

Weber, A.I., Pillow, J.W., 2017. Capturing the dynamical repertoire of single neurons with generalized linear models. Neural Comput. 29 (12), 3260–3289. https://doi.org/10.1162/neco_a_01021.

Wu, H., Chen, W., Zhao, F., Zhou, Q., Reinach, P.S., Deng, L., Ma, L., Luo, S., Srinivasalu, N., Pan, M., Hu, Y., Pei, X., Sun, J., Ren, R., Xiong, Y., Zhou, Z., Zhang, S., Tian, G., Fang, J., Zhou, X., 2018. Scleral hypoxia is a target for myopia control. Proc. Natl. Acad. Sci. U.S.A. 115 (30), E7091–E7100. https://doi.org/10.1073/pnas.1721443115.